Accelerating the photocatalytic water splitting in catalyst-dye complexes

Shao, Y.

CHAPTER 3

A Proton Acceptor near the Active Site Lowers Dramatically the O–O Bond Formation Energy Barrier

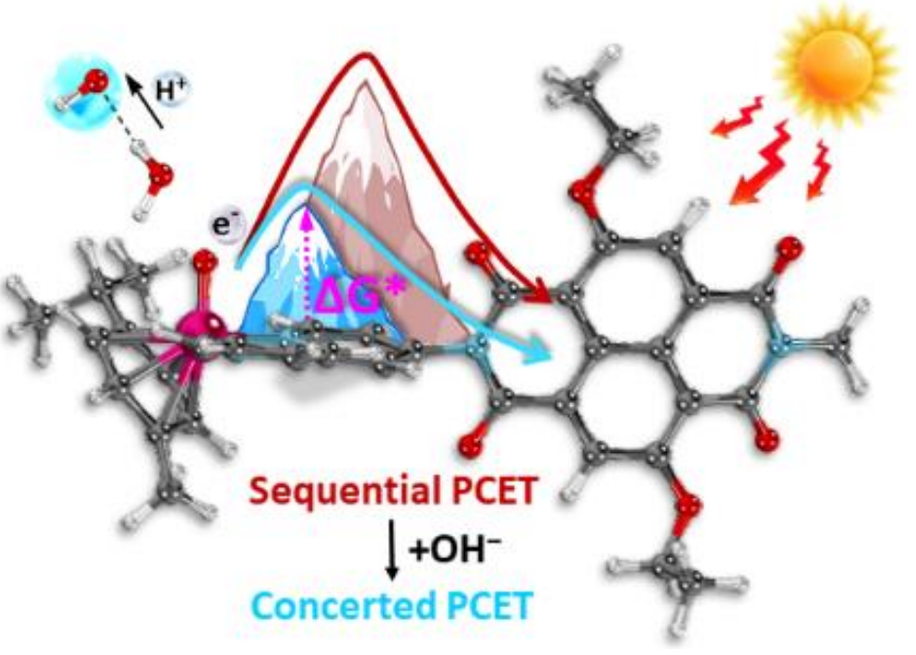

This chapter is based on:

Shao Yang, Huub J.M. de Groot, and Francesco Buda, *The Journal of Physical Chemistry Letters*, **2019**, 10, 7690-7697, DOI: 10.1021/acs.jpclett.9b02914.

3

Chapter 3

Abstract

The O–O bond formation process via water nucleophilic attack represents a thermodynamic and kinetic bottleneck in photocatalytic water oxidation because of the considerably high activation free energy barrier. It is of fundamental significance and challenging to find strategies to facilitate this reaction. The microscopic details of the photocatalytic water oxidation step involving the O–O bond formation in a catalyst–dye supramolecular complex are here elucidated by AIMD simulations in the presence of an extra proton acceptor. Introducing a proton acceptor group (OH^-) in the hydration shell near the catalytic active site accelerates the rate-limiting O–O bond formation by inducing a cooperative event proceeding via a concerted PCET mechanism and thus significantly lowering the activation free energy barrier. The in-depth insight provides a strategy for facilitating the photocatalytic water oxidation and for improving the efficiency of DS-PECs.

3.1. Introduction

Direct conversion of solar energy into storable fuels, as a credible alternative to fossil fuels, has long been considered as an attractive approach to meet long-term sustainable energy needs.[1-3] DS-PECs for solar-driven water splitting provide an opportunity to develop artificial photosynthetic devices by integrating visible light-absorbing sensitizers with WOCs or HECs on metal-oxide electrodes.[4-8] In DS-PECs, water is oxidized to oxygens and protons by photogenerated holes at the (photo-)anode whereas protons/CO_2 are reduced by photoinduced electrons at the (photo-)cathode to produce energy-rich H_2 or CO_2-derived fuels. The process is thermodynamically driven by the photooxidation of sensitizers which should be coupled with WOCs/HECs and anchored to a metal-oxide semiconductor surface.[9-13]

Although increasing effort has been devoted to developing efficient dye-sensitized photoanodes, the photocatalytic four-photon water oxidation half-reaction is still among the most crucial challenges throughout the entire process impeding the large-scale implementation of DS-PEC devices today.[9-10] Among the four PCET[14-15] steps involved in catalytic water oxidation, the O–O bond formation process represents a thermodynamic and kinetic bottleneck because of the considerably high activation free energy barrier, which is especially found when using mono-metallic catalysts that proceed via a water-nucleophilic attack mechanism.[16-19] Therefore, better understanding of the mechanism of O–O bond formation is currently a key issue that has attracted enormous interest in the past decades.[20-22] We recently explored *in silico* the whole photocatalytic water splitting cycle driven by a WOC–dye supramolecular complex $[(cy)Ru^{II}bpy(H_2O)]^{2+}$–NDI ($[Ru^{II}–OH_2]^{2+}$–NDI for short) solvated in explicit water by using AIMD simulations, which is indeed DFT-MD.[23-24]

Specifically, the third catalytic water oxidation step involving the O–O bond formation proceeded more likely via a sequential PCET mechanism (see red arrows in Scheme 3.1)[25] and exhibited an activation free energy barrier ΔG^* as high as 15.9 kcal mol^{-1} (~0.69 eV). Using transition state theory, this energy barrier translates into a reaction rate k = 15.7 s^{-1}.[24] On this time scale charge recombination from the semiconductor surface to the photooxidized dye becomes very likely, thus reducing the quantum efficiency of the process. It is

therefore of fundamental importance to find strategies that avoid high-energy intermediates in the sequential PCET process, which has been estimated to be substantially endothermic,[25-28] and thus facilitate the O–O bond formation.

Scheme 3.1. The four PCET steps between the catalytic intermediates (I_i) from I_1 to I_0 for water oxidation.[a]

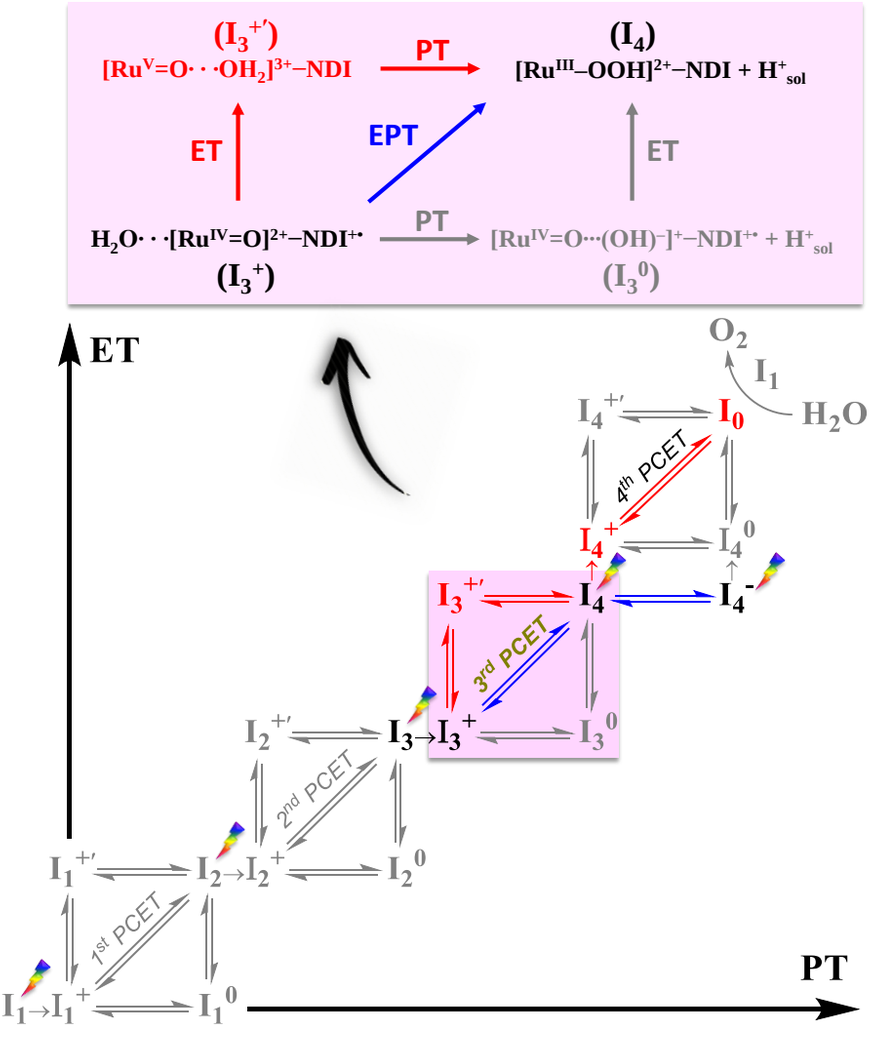

[a]It is assumed that each light flash induces the photooxidation of the NDI ($I_i \rightarrow I_i^+$ and $I_4^- \rightarrow I_4^o$): NDI → NDI$^{+\bullet}$. The vertical and horizontal double arrows correspond to the pathways of a sequential PCET mechanism, either ET from the WOC to the oxidized dye first ($I_i^+ \rightarrow I_i^{+\prime}$, $I_i^o \rightarrow I_{i+1}$, and $I_4^o \rightarrow I_0$: WOC–dye$^+$ → WOC$^+$–dye) or PT to the solvent first ($I_i^+ \rightarrow I_i^o$ and $I_4 \rightarrow I_4^-$). The diagonal double arrow denotes the concerted mechanism labeled as EPT (concerted electron-proton transfer). The favorable pathway of the third catalytic step established in ref. 24 is indicated in red and the catalytic pathway with the presence of OH^- as a proton acceptor is in blue. Intermediates investigated in the present study are shown in black. The ligand exchange $I_0 + H_2O \rightarrow I_1 + O_2$ is also indicated. H^+_{sol} represents the proton transferred to the solvent. The third step from I_3^+ to I_4, which is the main focus of this work, is specifically described in the top panel.

Scheme 3.2. Schematic structure of the ^{2}([(cy)Ru^{IV}bpy(O)]$^{2+}$–NDI$^{+\bullet}$) complex (^{2}([Ru^{IV}=O]$^{2+}$–NDI$^{+\bullet}$) for short) investigated in this work together with the attacking water molecule and the OH$^-$ in the vicinity of the Ru center.[a]

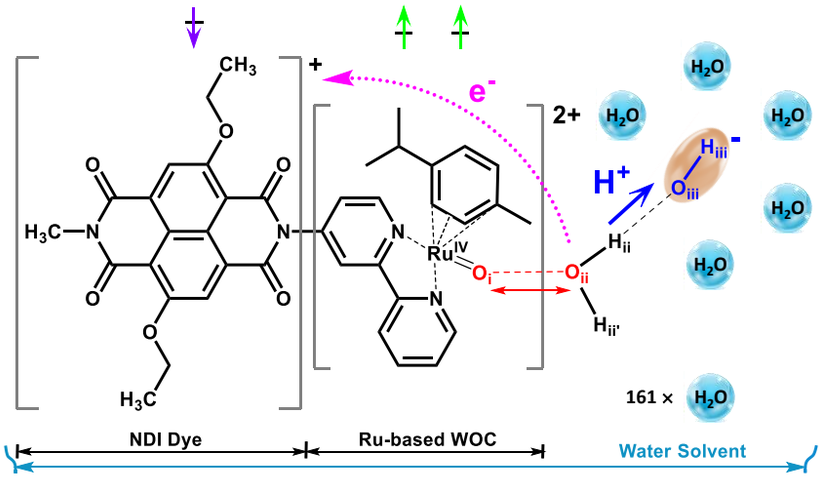

[a]The spin multiplicity value of 2*S*+1 = 2 (total spin *S* = 1/2) in this case corresponds to two unpaired *α* electrons (↑) localized on the catalyst and one unpaired *β* electron (↓) on the oxidized NDI$^{+\bullet}$. The red double-sided arrow indicates the reaction coordinate for the constrained MD simulations.

Although rate enhancement has been experimentally observed in catalytic water oxidation via ligand modification of WOCs[29-34] as well as solvent environmental tuning[35-40], the intrinsic mechanism at the molecular level is hidden behind the ensemble measurements. Computational studies play an important role in exploring the catalytic reaction mechanism and predicting the free energy change between reactant and product.[41-44] In particular, the catalytic water oxidation step involving the O–O bond formation process by single-site Ru metal complexes has been found to be 3 – 5 orders of magnitude faster with the addition of buffer bases owing to their involvement in either concerted atom-proton transfer (APT) or concerted electron-proton transfer (EPT) pathways.[35, 41-42] However, the thermodynamic and kinetic details of the mechanisms to accelerate the O–O bond formation are still unaccounted for, especially when considering a visible-light sensitizer coupled to the WOC and a more explicit description of solvent effects.

Here we report how the introduction of an extra OH$^-$ group as proton acceptor in the hydration shell near the catalytic active site facilitates the O–O bond formation process driven by the photooxidized dye in the *S* = 1/2 supramolecular complex ^{2}([Ru^{IV}=O]$^{2+}$–NDI$^{+\bullet}$) (see Scheme 3.2).

3.2 Computational Details

To obtain a quantitative description of the O–O bond formation process, we perform DFT-MD simulations using an orthorhombic box of dimensions 25.1 × 17.7 × 14.4 Å^3 with periodic boundary conditions containing the $[WOC]^{2+}$–dye solute, 161 water molecules, and one OH^- group. In plane wave based DFT-MD simulations with periodic boundary conditions, there is a spurious Coulomb interaction for charged systems introduced by the image charges. However, because of the large simulation box used and the screening from the explicit water molecules, the spurious effect of the periodic charges is estimated to be rather small (comparable to k_BT at room temperature) and does not affect significantly the conclusions of our simulations (see also Appendix 3.A.1.5). DFT-MD is an ideal approach to accurately describe chemical reactions in explicit solvent.[45] The solvent description allows accurate predictions of the reaction mechanisms and activation free energy barriers, since the solvent directly participates in the reaction, as already emphasized in similar studies.[46-49] All the simulations are performed at 300 K with the CPMD program[50], using GTH pseudopotentials for the transition metal[51] ruthenium and DCACP pseudopotentials for the remaining atoms[52], together with a plane wave cutoff of 70 Ry and the OPBE exchange-correlation functional[53] (see Appendix for more computational details). Considering the restrictions in the time scale of DFT-MD simulations, a constrained MD approach combined with thermodynamic integration was employed to compute the free energy profile along the O–O bond formation process.[54-56] The constrained reaction coordinate is the distance between the oxygen atoms O_i and O_{ii} indicated by the red double arrow in Scheme 3.2.

3.3. Results and Discussion

3.3.1 Inclusion and Equilibration of an OH^- Ion in the Simulation Box.

One water in the second solvation shell of the ruthenium center was deprotonated to create a hydroxide ion ($O_{iii}H_{iii}^-$) in the system at the very beginning of the simulation (see Scheme 3.2). If the OH^- ion is within ~8 Å of the Ru center, connected through a hydrogen bonded chain of water molecules,

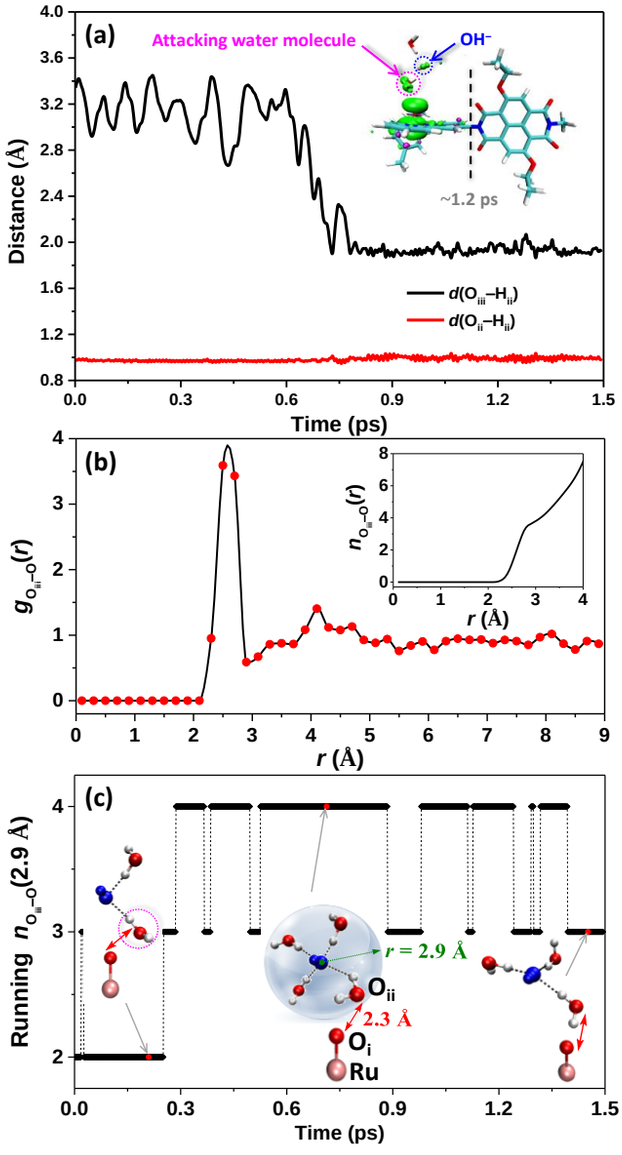

Figure 3.1. (a) Time evolution of the geometrical parameters $d(O_{ii}–H_{ii})$ (red line) and $d(O_{iii}\cdots H_{ii})$ (black line) along the initial equilibration MD trajectory corresponding to the constraint value $d(O_i\leftarrow O_{ii})$ = 2.3 Å (see Scheme 3.2 for the atomic labeling). The inset shows the spin density isosurface (green) computed at a snapshot taken at ~1.2 ps, in the triplet state with two unpaired α electrons localized on the catalyst and no unpaired electron on the NDI dye. Only the $^3([Ru^{IV}{=}O]^{2+}–NDI)$ complex, attacking water molecule (magenta dashed circle) and OH^- group (blue dashed circle) are shown explicitly. (b) Time-averaged O_{iii}–O radial distribution function and the corresponding integrated coordination number (inset in panel a) calculated for the O_{iii} of the OH^- group in the equilibration simulation, in which the O labels the water atoms as opposite to the hydroxyl one. (c) Running coordination number of OH^- along the equilibration MD trajectory. The insets in panel c show representative instantaneous snapshots for configurations with different coordination number, in which the OH^- group is indicated in blue. Only the involved water molecules including the attacking water molecule (magenta dashed ellipse) hydrogen-bonded to the OH^- group, the ruthenium metal center and the oxo ligand coordinating to it are shown explicitly. The red double sided arrow indicates the constrained distance $d(O_i\leftarrow O_{ii})$ = 2.3 Å.

the OH^- will move closer to the active site without any considerable energetic barrier by the Grotthuss mechanism.[57] Therefore the exact initial position of the OH^- is not so crucial and the mechanism will not change by placing the OH^- in the second hydration shell of the attacking water molecule. The reaction coordinate $d(O_i \leftarrow O_{ii})$ is initially fixed at 2.3 Å near the transition state according to the recently estimated reaction mechanism of O–O bond formation in a solvated system.[24] An initial DFT-MD simulation of about 1.5 ps is performed to equilibrate the local hydration environment around the OH^- group (see Appendix 3.A.1.4 for more computational details). During this equilibration run, a strong hydrogen bond between the OH^- group and the attacking water molecule is formed after about 0.8 ps with an average length $d(O_{iii} \cdots H_{ii}) \approx 1.9$ Å (see Figure 3.1a, black line). By tracking the spin density, two unpaired α electrons are observed to localize on the catalyst and no unpaired electron on the NDI dye (see Figure 3.1a, inset), which is consistent with the ground state of the $^3([Ru^{IV}{=}O]^{2+}$–NDI) intermediate known from previous investigations on this Ru-based catalyst.[24]

The time-averaged O_{iii}–O radial distribution function $g_{O_{iii}-O}(r)$ and the corresponding coordination number calculated in the equilibration simulation are presented in Figure 3.1b. The $g_{O_{iii}-O}(r)$ function shows a deep minimum at the O_{iii}–O distance r = ~2.9 Å, clearly revealing the existence of a first hydration shell of OH^-.[58] Accordingly, the running coordination number ($n_{O_{iii}-O}(2.9\ Å)$) of the OH^- group, defined as the number of water molecules with their oxygen atom within a radius of 2.9 Å around the oxygen atom (O_{iii}) of the OH^- group, is shown in Figure 3.1c. The $OH^-(H_2O)_4$ complex is observed to be the dominant solvation structure for OH^- during this simulation, with four water molecules primarily coordinated to the OH^- via hydrogen bonds (see Figure 3.1c, inset). This result is consistent with the coordination number obtained by integrating the first peak of the $g_{O_{iii}-O}(r)$ function (see Figure 3.1b, inset) and in agreement with the characteristic microscopic solvation structure of the OH^- group in aqueous solution observed in previous simulations.[58-64] All these evidences suggest a well-equilibrated solvation environment for the OH^- that represents a good starting point for the subsequent reaction mechanism investigation.

3.3.2 Photooxidation of the NDI and O–O Bond Formation

After this equilibration simulation, the photoinduced electron injection from the NDI to a TiO_2 semiconductor surface, *i.e.*, the photooxidation of the NDI dye, is mimicked by removing one electron from the simulation box. In previous work, we have demonstrated that the photoinduced electron injection is achieved on a time scale of ~1 ps.[23] To obtain a quantitative description of electron and proton dynamics, the variation of the total spin density localized on the NDI dye, and the time evolution of the distance between Ru and OH group (an O atom with only one H within a radius of 1.2 Å) along the constrained/free DFT-MD trajectory after photooxidation of NDI are collected in Figure 3.2. Initially, the photo-induced hole is localized on the oxidized $NDI^{+\bullet}$ (see Figure 3.2a and 3.2c), but it is quickly filled by an electron transferred from the attacking water molecule within 0.5 ps, leading to a minimum value around 0.1 of the spin density localized on NDI (see Figure 3.2a and 3.2e). Notice that during this ET the total spin $S = 1/2$ is assumed to be conserved. At the same time, the attacking water molecule transfers a proton (H_{ii} in Scheme 3.2) to the OH^- ion, which becomes a water molecule and no back reaction occurs (see Figure 3.2d and 3.2b blue line). This result indicates a cooperative event proceeding via a concerted PCET mechanism (see EPT in Scheme 3.1) that is completed within ~0.5 ps after the photooxidation of the NDI (see Figure 3.2a–3.2e).

In Figure 3.2e it is also apparent that the attacking water molecule has become an OH group carrying some spin density that indicates a strong radical character. One can indeed conclude that the hydroxide is first transferred close to the Ru(IV)=O, it acquires a radical character and thus generates a favorable condition for the O–O bond formation. The configuration shown in Figure 3.2e would be observed if the OH^- is placed initially as the direct attacking group next to the Ru(IV)=O. However, it is more appropriate to assume that the OH^- group will approach the active site in its more stable solvated complex as described in Figure 3.1. After short-term fluctuations, the spin density localized on the NDI stabilizes to an average value around 0.1 in the second half of the constrained MD simulation, indicating almost complete ET from the attacking water molecule to the oxidized $NDI^{+\bullet}$ (see Figure 3.2a).

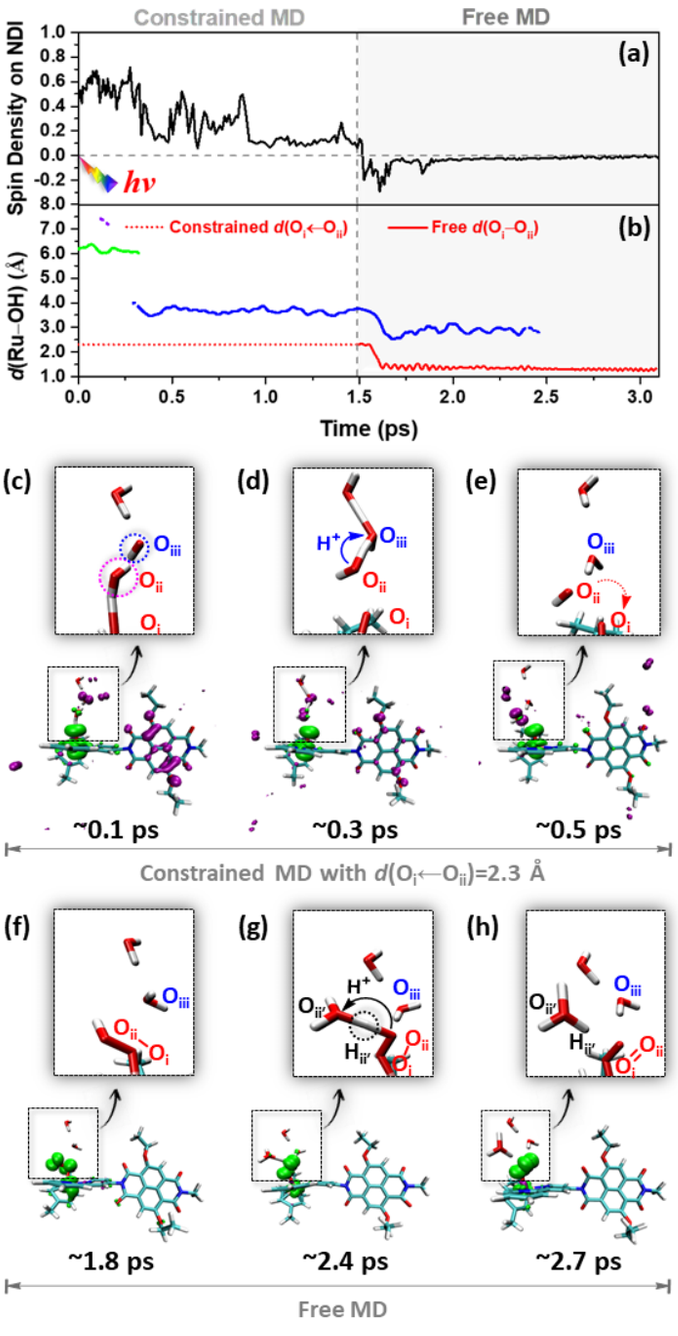

Figure 3.2 (a) The spin density integrated over the half of the simulation box that includes the NDI dye (right-hand side of the dashed black line in the inset of Figure 3.1a) along the constrained and free DFT-MD trajectories with the presence of OH^- group. An integrated spin density value of 1 corresponds to one unpaired β electron ($\downarrow$). (b) $d(O_i–O_{ii})$ distance during the constrained (red dotted line) and free (red solid line) MD trajectories. The green, purple, and blue lines show the instantaneous distance between the Ru and the OH group defined as an O atom with only one H atom within a radius of 1.2 Å. Different colors are used to underline when the OH is transferred from one hydration shell to another. The OH is initially in the second hydration shell at about 6 Å from the Ru (green line). The purple dots in the upper left corner indicate transient events in which a proton is accepted by a water molecule in the third hydration shell. Thus, the OH^- moves temporarily further away from the Ru complex and quickly jumps

back in the second hydration shell. After about 0.3 ps the proton is accepted from the attacking water and thus the OH moves closer to the Ru (blue line). (c)–(h) Spin density localization at different snapshots together with PT of third catalytic step (c→d→e), O–O bond formation process (e→f), and prior PT of fourth catalytic step (g→h) along the constrained/free MD trajectory shown in panels a and b. The labels refer to the time at which the snapshot has been taken. The snapshot taken at ~0.1 ps clearly indicates two unpaired α electrons (green spin density isosurface) localized on the catalyst and one unpaired β electron (purple spin density isosurface) on the oxidized $NDI^{+\bullet}$ dye. Only the WOC–dye complex, attacking water molecule (magenta dashed circle), OH^- group (blue dashed circle) and one nearby water molecule are shown explicitly (see enlargement in the insets). A small amount of spin density can be seen localized on a few water molecules due to transient solvent polarization effects.

This concerted PCET process occurs at the constrained reaction coordinate $d(O_i \leftarrow O_{ii})$ = 2.3 Å in the presence of the OH^- in the solvent. In contrast, without an additional proton acceptor the PCET occurs in a sequential (first ET, then PT, see red arrows in Scheme 3.1) mechanism and is completed only at $d(O_i \leftarrow O_{ii})$ = 1.8 Å.[24]

The release of the constraint between oxygens O_i and O_{ii} at ~1.5 ps enables the O–O bond formation, which proceeds in a very short time (within 0.2 ps) as the bond distance equilibrates at an average value $d(O_i–O_{ii})$ of ~1.36 Å (see red line in Figure 3.2b and 3.2f) (for comparison, the O–O bond length in molecular hydrogen peroxide is 1.47 Å), confirming the accomplishment of the rate-limiting catalytic step (see eq. 3.1). In eq. 3.1, H_2O_{sol} and OH^-_{sol} represent the attacking water molecule and hydroxide ion in the solvent, respectively.

3.3.3 Spontaneous Proton Transfer Following OOH Ligand Formation

After the formation of the $^2([Ru^{III}–OOH]^{2+}–NDI)$ intermediate, the free DFT-MD simulation shows that the $H_{ii'}$ of the hydroperoxyl ligand (see labeling in Scheme 3.2 and black dashed circle in Figure 3.2g) is strongly hydrogen-bonded to a neighboring water molecule. This hydrogen bond weakens the $O_{ii}–H_{ii'}$ bond and facilitates the proton ($H_{ii'}$) release from the Ru^{III}–OOH center.

$$^2([Ru^{IV}{=}O]^{2+}–NDI^{+\bullet}) \cdots H_2O_{sol} + OH^-_{sol} \xrightarrow{\text{Concerted PCET}} {}^2([Ru^{III}–OOH]^{2+}–NDI) + H_2O_{sol} \qquad (3.1)$$

This proton is further transferred into the water bulk through a specific hydrogen-bonding network and finally forms a $H_5O_2^+$ complex in the solvent after

$$^{2}([Ru^{III}\text{–}OOH]^{2+}\text{–NDI}) \cdots 2H_2O_{sol} \xrightarrow{PT} {}^{2}([Ru^{III}(O{=}O)]^{+}\text{–NDI}) + H_5O_2{}^{+}{}_{sol} \qquad (3.2)$$

~2.5 ps during this simulation (see Figure 3.2h and Figure A3.1 in Appendix). The last part of the FMD trajectory confirms the early formation of an O=O bond with an average $d(O_i\text{–}O_{ii})$ of ~1.29 Å (red line in Figure 3.2b, the O=O bond length in molecular O_2 is 1.21 Å for comparison) and a weakened Ru–O_i bond (see Figure A3.1a in Appendix). One triplet molecular O_2 can be produced and easily exchanged with a surrounding water molecule to generate the initial WOC state once the extra electron is transferred away from the Ru complex (see Scheme 3.1, $I_4^- \rightarrow I_4^o \rightarrow I_o$). These findings provide convincing evidence for a quite active intermediate with a hydroperoxyl ligand after the O–O bond formation process as well as a considerably thermodynamically facile fourth water oxidation step (see eq. 3.2, where $H_5O_2{}^{+}{}_{sol}$ represents the hydrated excess proton complex). Interestingly, the barrier-less PT, usually considered as thermodynamically favorable after ET,[65] proceeds spontaneously with no need for prior ET, emphasizing the possibility of rate enhancement in water oxidation catalysis by tuning solvent environment to allow prior or facilitated PT in the system. It is noticeable the analogy in the sequence of reaction steps predicted by the simulation after the photooxidation of the NDI (*i.e.*, PCET followed by PT) and those observed in the oxygen evolving complex of PSII after the third light flash leading to O_2 evolution.[2]

3.3.4 Activation Free Energy Barrier and Reaction Rate Evaluation

Additional exploration with a constrained reaction coordinate $d(O_i \leftarrow O_{ii})$ = 2.5 Å after the initial equilibration simulation discussed above is also carried out and reported for completeness in Appendix 3.A.3. It is found that the PCET step could still take place when elongating the reaction coordinate $d(O_i \leftarrow O_{ii})$ to 2.5 Å with the presence of OH^- as a proton acceptor in the solvent, although at a lower rate compared to the simulation with $d(O_i \leftarrow O_{ii})$ = 2.3 Å (within 1.2 ps after the photooxidation of NDI). However, rapid electron recombination is observed after the release of constraint, which induces the migration of the attacking water molecule away from the Ru^{IV}=O_i center and the subsequent back reaction of transferred proton to reproduce the original attacking water molecule (see Figure A3.2).

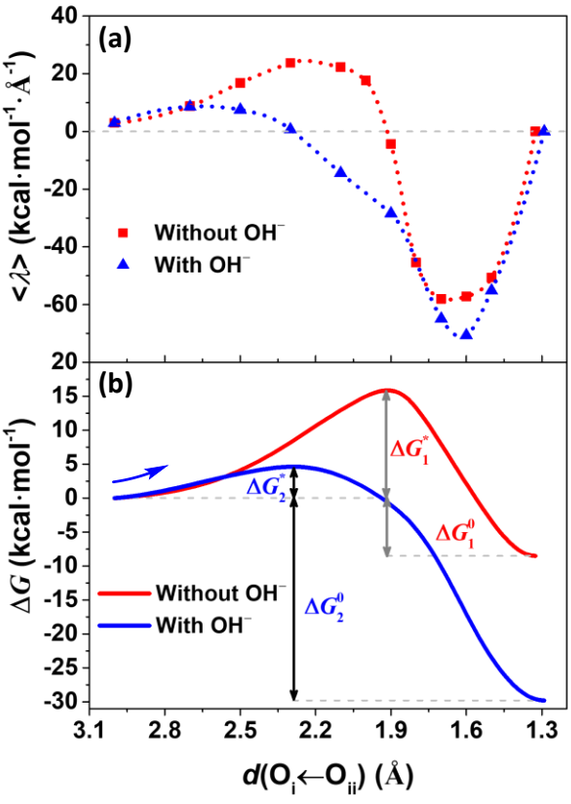

Figure 3.3. (a) Time-averaged constraint force represented by the Lagrangian multiplier $\langle\lambda\rangle$ computed for each constrained MD simulation as a function of the reaction coordinate $d(O_i{\leftarrow}O_{ii})$ with (blue triangles) and without (red squares) the OH^-, respectively. The Akima splines (100 points) is used to interpolate the mean forces. The mean force at the equilibrium distance $d(O_i{-}O_{ii})$ = 1.29 Å evaluated in the free MD has been set to 0. (b) Free energy profile along the reaction coordinate $d(O_i{\leftarrow}O_{ii})$ computed by thermodynamic integration with (blue line) and without (red line) the OH^-, respectively. The results obtained without the presence of OH^- in the solvent are from Ref. 24.

In order to quantify the significant role of OH^- as a proton acceptor in the solvent in facilitating the rate-limiting water oxidation step involving the O–O bond formation process, the reaction coordinate $d(O_i{\leftarrow}O_{ii})$ is constrained to a series of fixed values to estimate the free energy profile along this reaction pathway (see Appendix 3.A.1.3 for more details). Figures 3.3a (blue triangles) and 3.3b (blue line) present the time-averaged mean forces corresponding to the applied constraint and associated free energy profile estimated by thermodynamic integration, respectively. The value of $\langle\lambda\rangle_{2.3\ \text{Å}} \approx 0$ observed in Figure 3.3a indicates a transition state of this reaction with a O···O distance close to 2.3 Å, which well explains why the O–O bond formation cannot occur at $d(O_i{\leftarrow}O_{ii})$ = 2.5 Å. In Table 3.1, we summarize the thermodynamic parameters for this PCET step involving the O–O bond formation with and without OH^-.

Chapter 3

Noticeably, the calculated activation free energy barrier ΔG^* of this O–O bond formation process is dramatically lowered to ~4.3 kcal mol^{-1} (~0.19 eV) compared to the case without the presence of OH^- in the solvent ($\Delta G^* \approx 15.9$ kcal mol^{-1} (~0.69 eV)).[24]

Table 3.1. The calculated activation free energy barrier ΔG^* (in kcal mol^{-1}) and reaction driving force ΔG^o (in kcal mol^{-1}) with and without OH^- group as a proton acceptor. The last column shows the rate ratio (k_2/k_1) between the cases with (k_2 in s^{-1}) and without (k_1 in s^{-1}) the OH^- group.

Water Solvent	**ΔG^***	**ΔG^o**	**k_2/k_1**
Without OH^-[24]	15.9	−8.5	~2.83×10^8
With OH^-	4.3	−30.1	

This reaction step turns out to be significantly facilitated by introducing OH^- as proton acceptor near the active site to induce a concerted PCET mechanism. Moreover, the considerably larger driving force $\Delta G^o \approx -30.1$ kcal mol^{-1} (~1.31 eV) found with the OH^- can be partly attributed to the accomplishment of the spontaneous PT process after the formation of the hydroperoxyl ligand, which leads to a relatively stable intermediate $^2([Ru^{III}(O=O)]^+$–NDI) compared to $^2([Ru^{III}$–$OOH]^{2+}$–NDI).

The computed activation free energy barrier can be used to evaluate to what extent the introduction of OH^- group as a proton acceptor near the active site accelerates the rate of the O–O bond formation. According to standard transition state theory[66-68], the reaction rate k can be expressed as

$$k = A \cdot e^{-\frac{\Delta G^*}{RT}} \qquad (3.3)$$

One should keep in mind that in the DFT-MD simulations protons are treated classically and thus proton tunneling effects are neglected. In the current estimate, only the activation free energy barrier is considered as a main factor governing the reaction rate and the pre-exponential factor is regarded as constant. The calculated ratio of reactions rate ($k_2/k_1 \approx \sim 2.83 \times 10^8$) indicates an increase of over eight orders of magnitude for the O–O bond formation process in the presence of a OH^- as a proton acceptor near the active site (see Table 3.1), which is comparable with the experimental rate accelerations achieved by adding proton acceptor bases in the solution.[35, 42]

3.4. Conclusions

In conclusion, the explicit solvent and dynamic description obtained with the adiabatic DFT-MD modelling approach reveals that the photooxidation of the NDI dye covalently bound to a highly active mononuclear Ru-based WOC provides a sufficient driving force for the ET from the attacking water molecule to the oxidized $NDI^{+\bullet}$ dye and thus drives this photocatalytic water oxidation step. Introducing one OH^- group as a proton acceptor near the active site induces a cooperative event proceeding via a concerted PCET mechanism, dramatically lowers the activation free energy barrier and thus significantly accelerates the O–O bond formation.

The mechanistic insight into facilitated O–O bond formation process provides a strategy for the improvement of the performance of DS-PEC devices by straigthforward tuning of the solvent environment rather than developing novel catalysts for efficient water catalysis via tedious and costly synthesis technology. In this work we specifically use the OH^- group as a conceptual example, but this can be easily replaced by other proton acceptors that would be less detrimental to the WOC stability. Based on these results, we propose a design strategy for a DS-PEC architecture in which the catalyst layer is located in the proximity of an ion-exchange membrane. In particular one could use assembly strategies similar to solid-state water electrolysis cell with alkaline membranes in which the OH^- ions are transported to the catalyst layer through the anion exchange membrane and act as proton-withdrawing groups.[69]

Moreover, the decoupling of tuning of the proton chemical potential from tuning the electron chemical potential would be essential to the design of future optimal DS-PEC devices. This will facilitate the photocatalytic water oxidation and simultaneously the proton diffusion through the membrane for the purpose of efficient hydrogen production.[70]

3.5 References

[1] Lewis, N. S. *Science* **2007**, *315*, 798-801.
[2] Dau, H.; Zaharieva, I. *Acc. Chem. Res.* **2009**, *42*, 1861-1870.
[3] Nocera, D. G. *Acc. Chem. Res.* **2012**, *45*, 767-776.
[4] Li, L.; Duan, L.; Wen, F.; Li, C.; Wang, M.; Hagfeldt, A.; Sun, L. *Chem. Commun.* **2012**, *48*, 988-990.
[5] Grätzel, M. *Nature* **2001**, *414*, 338-344.
[6] Kohl, S. W.; Weiner, L.; Schwartsburd, L.; Konstantinovski, L.; Shimon, L. J. W.; Ben-David, Y.; Iron, M. A.; Milstein, D. *Science* **2009**, *324*, 74-77.
[7] Xu, P.; Huang, T.; Huang, J.; Yan, Y.; Mallouk, T. E. *Proc. Natl. Acad. Sci. U.S.A.* **2018**, *115*, 6946-6951.
[8] Yu, Z.; Li, F.; Sun, L. *Energy Environ. Sci.* **2015**, *8*, 760-775.
[9] Swierk, J. R.; Mallouk, T. E. *Chem. Soc. Rev.* **2013**, *42*, 2357-2387.
[10] Ding, X.; Zhang, L.; Wang, Y.; Liu, A.; Gao, Y. *Coord. Chem. Rev.* **2018**, *357*, 130-143.
[11] Gibson, E. A. *Chem. Soc. Rev.* **2017**, *46*, 6194-6209.
[12] Xu, P.; McCool, N. S.; Mallouk, T. E. *Nano Today* **2017**, *14*, 42-58.
[13] Wang, D.; Eberhart, M. S.; Sheridan, M. V.; Hu, K.; Sherman, B. D.; Nayak, A.; Wang, Y.; Marquard, S. L.; Dares, C. J.; Meyer, T. J. *Proc. Natl. Acad. Sci. U.S.A.* **2018**, *115*, 8523-8528.
[14] Gagliardi, C. J.; Vannucci, A. K.; Concepcion, J. J.; Chen, Z.; Meyer, T. J. *Energy Environ. Sci.* **2012**, *5*, 7704-7717.
[15] Hammes-Schiffer, S. *Chem. Rev.* **2010**, *110*, 6937-6938.
[16] Yang, X.; Hall, M. B. *J. Am. Chem. Soc.* **2010**, *132*, 120-130.
[17] Concepcion, J. J.; Tsai, M.-K.; Muckerman, J. T.; Meyer, T. J. *J. Am. Chem. Soc.* **2010**, *132*, 1545-1557.
[18] Privalov, T.; Sun, L.; Åkermark, B.; Liu, J.; Gao, Y.; Wang, M. *Inorg. Chem.* **2007**, *46*, 7075-7086.
[19] Lin, X.; Hu, X.; Concepcion, J. J.; Chen, Z.; Liu, S.; Meyer, T. J.; Yang, W. *Proc. Natl. Acad. Sci. U.S.A.* **2012**, *109*, 15669-15672.
[20] Cao, R.; Lai, W.; Du, P. *Energy Environ. Sci.* **2012**, *5*, 8134-8157.
[21] Shaffer, D. W.; Xie, Y.; Szalda, D. J.; Concepcion, J. J. *J. Am. Chem. Soc.* **2017**, *139*, 15347-15355.
[22] Meyer, T. J.; Sheridan, M. V.; Sherman, B. D. *Chem. Soc. Rev.* **2017**, *46*, 6148-6169.
[23] Monti, A.; de Ruiter, J. M.; de Groot, H. J. M.; Buda, F. *J. Phys. Chem. C* **2016**, *120*, 23074-23082.
[24] Shao, Y.; de Ruiter, J. M.; de Groot, H. J. M.; Buda, F. *J. Phys. Chem. C* **2019**, *123*, 21403-21414.
[25] Hammes-Schiffer, S. *J. Am. Chem. Soc.* **2015**, *137*, 8860-8871.
[26] Iordanova, N.; Hammes-Schiffer, S. *J. Am. Chem. Soc.* **2002**, *124*, 4848-4856.
[27] Hatcher, E.; Soudackov, A. V.; Hammes-Schiffer, S. *J. Am. Chem. Soc.* **2004**, *126*, 5763-5775.
[28] Horvath, S.; Fernandez, L. E.; Soudackov, A. V.; Hammes-Schiffer, S. *Proc. Natl. Acad. Sci. U.S.A.* **2012**, *109*, 15663-15668.
[29] Maji, S.; Vigara, L.; Cottone, F.; Bozoglian, F.; Benet-Buchholz, J.; Llobet, A. *Angew. Chem., Int. Ed.* **2012**, *51*, 5967-5970.
[30] Garrido-Barros, P.; Funes-Ardoiz, I.; Drouet, S.; Benet-Buchholz, J.; Maseras, F.; Llobet, A. *J. Am. Chem. Soc.* **2015**, *137*, 6758-6761.
[31] Wilson, A. D.; Newell, R. H.; McNevin, M. J.; Muckerman, J. T.; Rakowski DuBois, M.; DuBois, D. L. *J. Am. Chem. Soc.* **2006**, *128*, 358-366.
[32] Helm, M. L.; Stewart, M. P.; Bullock, R. M.; DuBois, M. R.; DuBois, D. L. *Science* **2011**, *333*, 863-866.

[33] Bediako, D. K.; Solis, B. H.; Dogutan, D. K.; Roubelakis, M. M.; Maher, A. G.; Lee, C. H.; Chambers, M. B.; Hammes-Schiffer, S.; Nocera, D. G. *Proc. Natl. Acad. Sci. U.S.A.* **2014**, *111*, 15001-15006.
[34] Solis, B. H.; Maher, A. G.; Honda, T.; Powers, D. C.; Nocera, D. G.; Hammes-Schiffer, S. *ACS Catal.* **2014**, *4*, 4516-4526.
[35] Song, N.; Concepcion, J. J.; Binstead, R. A.; Rudd, J. A.; Vannucci, A. K.; Dares, C. J.; Coggins, M. K.; Meyer, T. J. *Proc. Natl. Acad. Sci. U.S.A.* **2015**, *112*, 4935-4940.
[36] Norris, M. R.; Concepcion, J. J.; Fang, Z.; Templeton, J. L.; Meyer, T. J. *Angew. Chem., Int. Ed.* **2013**, *52*, 13580-13583.
[37] Coggins, M. K.; Zhang, M.-T.; Chen, Z.; Song, N.; Meyer, T. J. *Angew. Chem., Int. Ed.* **2014**, *53*, 12226-12230.
[38] Chen, Z.; Concepcion, J. J.; Song, N.; Meyer, T. J. *Chem. Commun.* **2014**, *50*, 8053-8056.
[39] Stewart, D. J.; Concepcion, J. J.; Brennaman, M. K.; Binstead, R. A.; Meyer, T. J. *Proc. Natl. Acad. Sci. U.S.A.* **2013**, *110*, 876-880.
[40] Vannucci, A. K.; Alibabaei, L.; Losego, M. D.; Concepcion, J. J.; Kalanyan, B.; Parsons, G. N.; Meyer, T. J. *Proc. Natl. Acad. Sci. U.S.A.* **2013**, *110*, 20918-20922.
[41] Matheu, R.; Ertem, M. Z.; Benet-Buchholz, J.; Coronado, E.; Batista, V. S.; Sala, X.; Llobet, A. *J. Am. Chem. Soc.* **2015**, *137*, 10786-10795.
[42] Chen, Z.; Concepcion, J. J.; Hu, X.; Yang, W.; Hoertz, P. G.; Meyer, T. J. *Proc. Natl. Acad. Sci. U.S.A.* **2010**, *107*, 7225-7229.
[43] Xie, Y.; Shaffer, D. W.; Lewandowska-Andralojc, A.; Szalda, D. J.; Concepcion, J. J. *Angew. Chem., Int. Ed.* **2016**, *55*, 8067-8071.
[44] Govindarajan, N.; Tiwari, A.; Ensing, B.; Meijer, E. J. *Inorg. Chem.* **2018**, *57*, 13063-13066.
[45] Marx, D.; Hutter, J. *Ab initio molecular dynamics: basic theory and advanced methods;* Cambridge University Press: Cambridge, U.K., 2009.
[46] Handgraaf, J.-W.; Meijer, E. J. *J. Am. Chem. Soc.* **2007**, *129*, 3099-3103.
[47] Ma, C.; Piccinin, S.; Fabris, S. *ACS Catal.* **2012**, *2*, 1500-1506.
[48] Pavlova, A.; Meijer, E. J. *ChemPhysChem* **2012**, *13*, 3492-3496.
[49] Vallés-Pardo, J. L.; Guijt, M. C.; Iannuzzi, M.; Joya, K. S.; de Groot, H. J. M.; Buda, F. *ChemPhysChem* **2012**, *13*, 140-146.
[50] CPMD, http://www.cpmd.org, Copyright IBM Corp., 1990-2019, Copyright MPI für Festkörperforschung Stuttgart, 1997-2001.
[51] Hartwigsen, C.; Goedecker, S.; Hutter, J. *Phys. Rev. B* **1998**, *58*, 3641-3662.
[52] Lin, I. C.; Coutinho-Neto, M. D.; Felsenheimer, C.; von Lilienfeld, O. A.; Tavernelli, I.; Rothlisberger, U. *Phys. Rev. B* **2007**, *75*, No. 205131.
[53] Swart, M.; Ehlers, A. W.; Lammertsma, K. *Mol. Phys.* **2004**, *102*, 2467-2474.
[54] Ciccotti, G.; Ferrario, M. *Mol. Simul.* **2004**, *30*, 787-793.
[55] Ensing, B.; Meijer, E. J.; Blöchl, P. E.; Baerends, E. J. *J. Phys. Chem. A* **2001**, *105*, 3300-3310.
[56] Costanzo, F.; Della Valle, R. G. *J. Phys. Chem. B* **2008**, *112*, 12783-12789.
[57] de Ruiter, J. M. Explorations of water oxidation catalysis in explicit solvent. Ph.D. Thesis, Leiden University, October 2018.
[58] Lee, S. H.; Rasaiah, J. C. *Mol. Simul.* **2010**, *36*, 69-73.
[59] Crespo, Y.; Hassanali, A. *J. Phys. Chem. Lett.* **2015**, *6*, 272-278.
[60] Tuckerman, M.; Laasonen, K.; Sprik, M.; Parrinello, M. *J. Chem. Phys.* **1995**, *103*, 150-161.
[61] Tuckerman, M.; Laasonen, K.; Sprik, M.; Parrinello, M. *J. Phys. Chem.* **1995**, *99*, 5749-5752.
[62] Chen, B.; Ivanov, I.; Park, J. M.; Parrinello, M.; Klein, M. L. *J. Phys. Chem. B* **2002**, *106*, 12006-12016.
[63] Botti, A.; Bruni, F.; Imberti, S.; Ricci, M. A.; Soper, A. K. *J. Chem. Phys.* **2004**, *120*, 10154-10162.
[64] Agmon, N.; Bakker, H. J.; Campen, R. K.; Henchman, R. H.; Pohl, P.; Roke, S.; Thämer, M.; Hassanali, A. *Chem. Rev.* **2016**, *116*, 7642-7672.

[65] de Ruiter, J. M.; de Groot, H. J. M.; Buda, F. *ChemCatChem* **2018**, *10*, 4594-4601.
[66] Eyring, H. *J. Chem. Phys.* **1935**, *3*, 107-115.
[67] Laidler, K. J.; King, M. C. *J. Phys. Chem.* **1983**, *87*, 2657-2664.
[68] Pollak, E.; Talkner, P. *Chaos* **2005**, *15*, No. 026116.
[69] Leng, Y.; Chen, G.; Mendoza, A. J.; Tighe, T. B.; Hickner, M. A.; Wang, C.-Y. *J. Am. Chem. Soc.* **2012,** *134*, 9054-9057.
[70] Achtyl, J. L.; Unocic, R. R.; Xu, L.; Cai, Y.; Raju, M.; Zhang, W.; Sacci, R. L.; Vlassiouk, I. V.; Fulvio, P. F.; Ganesh, P.; et al. *Nat. Commun.* **2015**, *6*, No. 6539.

3.A. Appendix

3.A.1. Computational Details

3.A.1.1 Geometry Optimization at DFT Level

The initial geometry of the WOC–dye complex was optimized at the DFT level employing the OPBE exchange-correlation functional[1] and the TZP basis set.[2] The OPBE functional has shown to be accurate in describing transition-metal complexes, including Ru-based WOCs.[3-6] In the geometry optimization, the continuous solvation model COSMO[7-8] for water was used. These calculations are performed with the ADF software package.[9-10]

3.A.1.2 Simulation Box

To obtain a realistic description of the catalytic reaction steps, the solvent was explicitly introduced in the simulations. The solvent environment for the CPMD simulations was generated using Discovery Studio 2.5.[11] The solvent was equilibrated for 0.2 ns using the TIP3P model implemented in the CHARMM force field and CFF partial charge parameters at 300 K,[12] while the $[WOC]^{2+}$–dye complex was kept fixed. The volume was then adjusted using constant pressure for 0.2 ns, after which the system was further allowed to evolve with constant volume for 2 ns. Periodic boundary conditions are applied with a time step of δt = 5 a.u. (1 a.u. = 0.0242 fs).

3.A.1.3 Free Energy Profile

To estimate the free energy profile of catalytic reaction steps that are unlikely to occur spontaneously during the typical AIMD simulation time scale, constrained MD and the so-called Blue Moon approach were employed as a rare event simulation technique.[13-15] The reaction coordinate (in this case the distance between two oxygen atoms O_i and O_{ii}, $d(O_i \leftarrow O_{ii})$, as shown in Scheme 3.1) is constrained to a series of fixed values x in range of 3.0 – 1.5 Å after the initial equilibrium simulation and subsequent photooxidation of NDI along this facilitated reaction pathway. A time-averaged constraint force $\langle\lambda\rangle_x$ for each value of the reaction coordinate x is obtained, which should be equal to zero at an equilibrium or transition state. The free energy change for this promoted catalytic step is then established by interpolating the mean forces with a 100-point Akima splines function and integrating the signed forces $\langle\lambda\rangle_x$ along the reaction path.[16-

[19] Trajectory analysis and visualization for the CPMD output were carried out using VMD program.[20-21]

3.A.1.4 Initial AIMD Equilibration Simulation

An initial AIMD simulation of about 1.5 ps is performed to equilibrate the local hydration environment around the OH^- group. In particular, the coordination number of the oxygen atom (O_{iii}) belonging to the OH^- group was constrained to one within a radius of 1.2 Å during this simulation to maintain the geometry of the OH^- group and prevent its diffusion via the hydrogen-bonding network.[22]

3.A.1.5 Effect of Periodic Boundary Conditions

In plane wave based DFT-MD simulations the periodic boundary conditions introduce a spurious Coulomb interaction for charged systems due to the image charges. In our work we compared the free energy profiles for two DFT-MD simulations with and without a OH^- ion. The total charge of the system is 2^+ or 3^+ in these two cases, respectively. The error introduced by the spurious Coulomb interaction can be estimated by considering the size of the MD box (25.1 × 17.7 × 14.4 $Å^3$) and the fact that the MD simulation box contains 161 water molecules that will strongly screen the spurious Coulomb interaction. A rough estimate of the Coulomb potential generated by a positive charge that takes into account the length of the box and the relative permittivity of water gives a value of ~0.46 kcal mol^{-1} for 2^+ and ~0.69 kcal mol^{-1} for 3^+, respectively. These energies are quite small and comparable to the thermal energy k_BT at room temperature (~0.59 kcal mol^{-1}). Moreover, these energies are at least one order of magnitude smaller than the computed free energy changes in the two systems considered (see Table 3.1 in chapter 3). We can therefore conclude that the error introduced by the periodic boundary conditions does not affect significantly the conclusions of our work.

3.A.2. Prior PT of the fourth Catalytic Water Oxidation Step

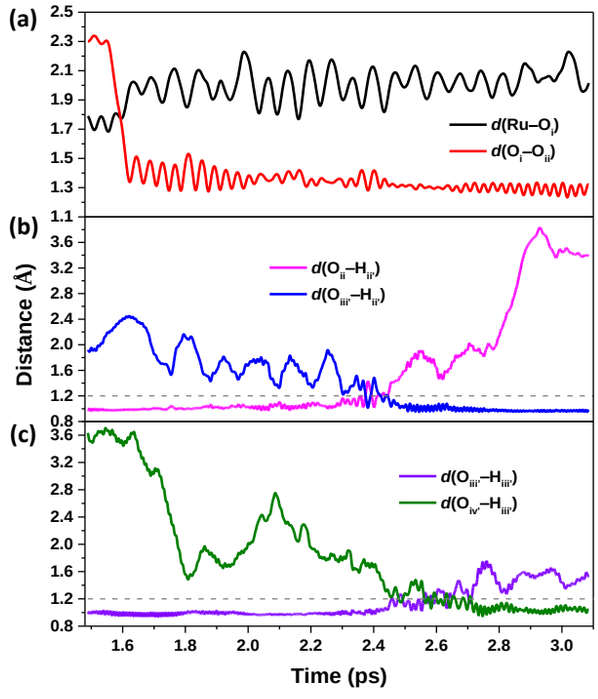

Figure A3.1. Time evolution of the geometrical parameters along the FMD trajectory after the third catalytic water oxidation step. The time range is consistent with Figure 3.2b

3.A.3. Exploration with Constrained Reaction Coordinate $d(O_i \leftarrow O_{ii})$ = 2.5 Å

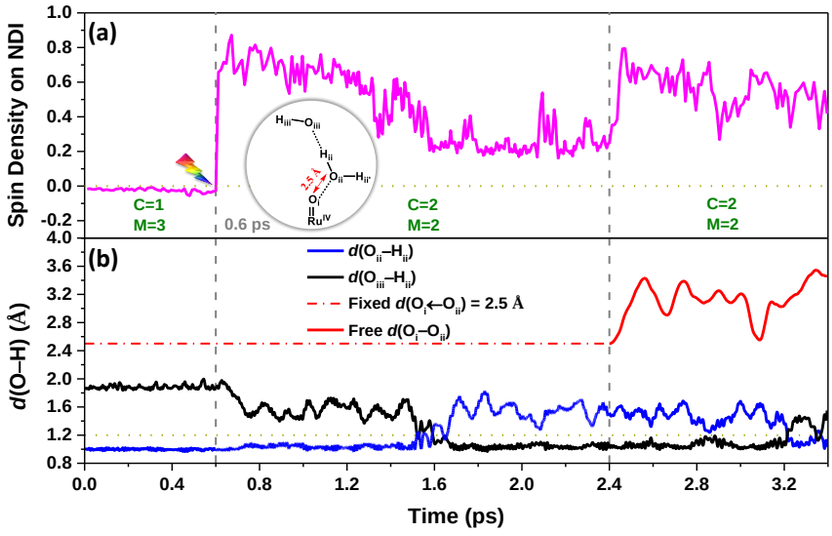

Figure A3.2. (a) The spin density integrated over the half of the simulation box including the NDI along the constrained and FMD trajectories. An integrated spin density value of 1 corresponds to one unpaired β electron. The red double sided arrow indicates the reaction coordinate $d(O_i \leftarrow O_{ii})$ = 2.5 Å. Grey dashed line at 0.6 ps: the photooxidation of NDI. Grey dashed line at 2.4 ps: remove constraint. (b) Time evolution of the geometrical parameters $d(O_i–O_{ii})$, $d(O_{ii}–H_{ii})$, and $d(O_{iii}–H_{ii})$ along the constrained and free MD trajectories. Inset shows a the schematic structure of the attacking water molecule and the extra OH^-.

3.A.4. References

[1] Swart, M.; Ehlers, A. W.; Lammertsma, K. *Mol. Phys.* **2004**, *102*, 2467-2474.
[2] Monti, A.; de Ruiter, J. M.; de Groot, H. J. M.; Buda, F. *J. Phys. Chem. C* **2016**, *120*, 23074-23082.
[3] Carvalho, A. T. P.; Swart, M. *J. Chem. Inf. Model.* **2014**, *54*, 613-620.
[4] Groenhof, A. R.; Ehlers, A. W.; Lammertsma, K. *J. Am. Chem. Soc.* **2007**, *129*, 6204-6209.
[5] Conradie, J.; Ghosh, A. *J. Chem. Theory Comput.* **2007**, *3*, 689-702.
[6] Vallés-Pardo, J. L.; Guijt, M. C.; Iannuzzi, M.; Joya, K. S.; de Groot, H. J. M.; Buda, F. *ChemPhysChem* **2012**, *13*, 140-146.
[7] Klamt, A. *J. Phys. Chem.* **1995**, *99*, 2224-2235.
[8] Klamt, A.; Jonas, V. *J. Chem. Phys.* **1996**, *105*, 9972-9981.
[9] te Velde, G.; Bickelhaupt, F. M.; Baerends, E. J.; Fonseca Guerra, C.; van Gisbergen, S. J. A.; Snijders, J. G.; Ziegler, T. *J. Comput. Chem.* **2001**, *22*, 931-967.
[10] ADF2017, SCM. Theoretical Chemistry, Vrije Universiteit, Amsterdam, The Netherlands, http://www.scm.com.
[11] Accelrys Sofrware Inc. *Discovery studio modeling environment*, Accelrys Sofrware Inc.: San Diego, 2012.
[12] Brooks, B. R.; Bruccoleri, R. E.; Olafson, B. D.; States, D. J.; Swaminathan, S.; Karplus, M. *J. Comput. Chem.* **1983**, *4*, 187-217.
[13] Ciccotti, G.; Ferrario, M. *Mol. Simul.* **2004**, *30*, 787-793.
[14] Ensing, B.; Meijer, E. J.; Blöchl, P. E.; Baerends, E. J. *J. Phys. Chem. A* **2001**, *105*, 3300-3310.
[15] Costanzo, F.; Della Valle, R. G. *J. Phys. Chem. B* **2008**, *112*, 12783-12789.
[16] Otter, W. K. d.; Briels, W. J. *J. Chem. Phys.* **1998**, *109*, 4139-4146.
[17] Sprik, M.; Ciccotti, G. *J. Chem. Phys.* **1998**, *109*, 7737-7744.
[18] Bernasconi, L.; Baerends, E. J.; Sprik, M. *J. Phys. Chem. B* **2006**, *110*, 11444-11453.
[19] Bernasconi, L.; Kazaryan, A.; Belanzoni, P.; Baerends, E. J. *ACS Catal.* **2017**, *7*, 4018-4025.
[20] Humphrey, W.; Dalke, A.; Schulten, K. *J. Mol. Graphics* **1996**, *14*, 33-38.
[21] VMD – Visual Molecular Dynamics. *Theoretical Chemistry and Computational Biophysics Group,* University of Illinois: Urbana, 2016.
[22] Crespo, Y.; Hassanali, A. *J. Phys. Chem. Lett.* **2015**, *6*, 272-278.